MOLECULAR IMAGING AND BIOLOGY

Mol Imaging Biol (2019) 21:1044–1053
DOI: 10.1007/s11307-019-01340-7

Published Online: 8 March 2019

WMIS World Molecular Imaging Society

Check for updates

RESEARCH ARTICLE

In Vivo Pharmacokinetics Assessment of Indocyanine Green-Loaded Nanoparticles in Tumor Tissue with a Dynamic Diffuse Fluorescence Tomography System

Yanqi Zhang,[1] Limin Zhang,[1,2] Guoyan Yin,[1] Wenjuan Ma,[3] Jiao Li,[1,2] Zhongxing Zhou,[1,2] Feng Gao[1,2]

[1]*School of Precision Instrument and Optoelectronics Engineering, Tianjin University, Tianjin, 300072, China*
[2]*Tianjin Key Laboratory of Biomedical Detecting Techniques and Instruments, Tianjin, 300072, China*
[3]*Cancer Institute and Hospital, Tianjin Medical University, Tianjin, 300060, China*

Abstract

Purpose: The purpose of this study was to show a systematic strategy for assessing the pharmacokinetics of indocyanine green (ICG)-loaded nanoparticles in the tumor tissue based on a dynamic diffuse fluorescence tomography (DFT) system.

Procedures: Twelve-seven-week-old male Balb/c nude mice bearing HepG2/ADR hepatocellular carcinoma were randomly divided into four groups ($n = 3$ per group). Four hundred microliters of three types of ICG-loaded nanoparticles (content of ICG: 50 μg/ml) and free ICG (50 μg/ml) was intravenously injected into the mice in each group, respectively. Afterwards, the real-time tomographic images on the spatial level were acquired at 2–11 min, 30 min, 1, 2, 3, 4, 6, 8, 10, 12, and 24 h post-injection, and pharmacokinetic rates were derived for semi-quantitative assessment of the pharmacokinetics of nanoparticles at the tumor site using our proposed pharmacokinetic analysis method.

Results: The results obtained from our proposed dynamic DFT experiment demonstrated the distribution of different ICG formulations on the spatial level and enabled the semi-quantitative analysis of the pharmacokinetics of nanoparticles in the tumor tissue.

Conclusions: The obtained pharmacokinetic rates effectively reflected the metabolic processes of nanoparticles in the tumor tissue, which proves to be beneficial for the development of tumor diagnosis and therapy.

Key words: Pharmacokinetics, Indocyanine green, Nanoparticles, Diffuse fluorescence tomography

Introduction

Nano-based drugs represent a promising pathway for enhancing the therapeutic index of chemotherapeutic drugs with reduced side effects, thereby potentially improving the quality of life for cancer patients [1–3]. Compared to free drugs, nano-based drugs offer various advantages such as a

Correspondence to: Limin Zhang; *e-mail:* zhanglm@tju.edu.cn, Feng Gao; *e-mail:* gaofeng@tju.edu.cn

high loading capacity, efficient protection of bioactive drugs, and distinct *in vivo* pharmacokinetic pathways [4].

When designing new nano-drugs, the evaluation of biodistribution and pharmacokinetics constitutes important preliminary data for the understanding of drug performance in biomedical tissues. In preclinical trials, traditional *in vitro* methods are generally used by sacrificing subsets of animals (often mice) at different time points to collect plasma and measure the drug concentration in each [5, 6]. With this information, the concentration-time curve for the pharmacokinetic analysis can be determined by using a high number of replicates at each time point for increasing the statistical power. For example, Song et al. have adopted inductively coupled plasma mass spectrometry (ICP-MS) to measure concentrations of the interior label Pt in the plasma for reflecting the metabolic behavior of a drug in mice bearing a subcutaneous xenograft tumor [6]. Conversely, *in vivo* methods can track the metabolic progress of the drug in a non-destructive manner within a single animal at multiple time points. This method may be beneficial for reducing cost and individual differences [7, 8]. Presently, fluorescence imaging constitutes one of the most fundamental paradigms, providing insights into either organism-drug interactions or pharmacological mechanisms by fluorescent labeling of biomolecules or drugs. Correspondingly, the fate of administered drugs can be reflected by detecting the pathway of the probes and measuring the relative fluorescence intensities in various tissues. Currently, most commercially available fluorescence imaging devices for live small animals offer the ability to continuously show the planar hierarchy distribution of fluorescence by charge-coupled device (CCD) imaging [9–11]. However, planar images represent the superposition of fluorescence signals from multiple depths, thus enabling the qualitative or semi-quantitative characterization of fluorescence intensities at depths of only a few millimeters.

To the best of our knowledge, diffuse fluorescence tomography (DFT) is able to three-dimensionally and quantitatively retrieve fluorescence distribution. The method offers numerous advantages including a non-invasive and radiation-free analysis, lower cost than common devices available to date and high sensitivity [12, 13]. Currently, most of the prototype systems developed for DFT are unsuitable for capturing fast-changing signals due to a particularly long image acquisition time. To overcome this limitation, dynamic DFT has been developed to record a sequence of tomographic images at different time intervals. Thus, the method may aid in a better understanding of the complete dynamic course of absorption, distribution, and elimination of fluorescence agents in biological tissues [14]. To date, some novel types of fluorescent probes and reporter technologies have been successfully developed, while indocyanine green (ICG) with peak excitation and fluorescence emission wavelengths of about 780 nm and 830 nm, respectively, remains a commonly used fluorescence agent as the only fluorescent dye certified by the United States Food and Drug Administration [15, 16]. For example, Burak et al. acquired a sequence of ICG concentration images of breast tumors using a CCD-based DFT system and further obtained pharmacokinetic rate images employing a two-compartment model [17]. Meanwhile, Bai et al. estimated the ICG pharmacokinetic rates of mouse liver with a hybrid imaging system of CCD-based DFT and X-ray computed tomography [18]. As one of the commonly used detection devices in DFT system, CCD can rapidly detect optical signal of one projection and achieve a high spatial resolution owing to large amounts of photosensitive elements. However, it is problematic and costly to acquire adequate signal-to-noise ratio over a complete 360° projections. An alternative is to adopt fiber-based detection model combined with an array of photomultiplier tubes (PMTs) or photodiodes and photon counting technique. This model is able to obtain high detection sensitivity and wide dynamic measurement range, which effectively compensates for its limitation in spatial sampling density by increasing the angle of view for one projection collection. In previous studies on ICG pharmacokinetics in the mouse liver, considering the poor quantum efficiency (0.016) of ICG and the fast metabolism of ICG in the liver, we have proposed a dynamic DFT system by combining PMTs and photon counting techniques for capturing fast-changing signal and designed a CT-analogous scanning mode to effectively improve spatial sampling resolution [19]. Additionally, a serial-to-parallel measurement strategy for achieving a tradeoff between the time resolution and the cost-effectiveness was adopted, where acquiring a complete frame of data can be performed by optically switching four parallel PMT photon-counting channels to eight detection sites sequentially.

Herein, we report a systematic strategy for the *in vivo* and semi-quantitative assessment of the pharmacokinetics of ICG-loaded nanoparticles in a mouse tumor model based on our proposed DFT system. In this work, the biodistribution of three types of lab-designed ICG-loaded nanoparticles and free ICG in mice with epidermal tumors were imaged using dynamic DFT. Furthermore, the pharmacokinetics of these nanoparticles were analyzed by extracting the pharmacokinetic rates from the reconstructed ICG concentration-time curves of tumor regions based on a two-compartment model. The experimental results demonstrated the feasibility of the dynamic system for monitoring the nanoparticle localization and following the nanoparticle activity in the tumor tissue. In addition, the obtained pharmacokinetic rates could be used to effectively reflect the metabolic progress of nanoparticles in the tumor tissues.

Materials and Methods

Materials

ICG was purchased from Liaoning Tianyi Biological Pharmaceutical Co., Ltd. (Liaoning, China). The fluorescent probe was encapsulated into three different types of nanoparticles as follows: (1) ICG-loaded biodegradable nanoparticles self-assembled from two copolymers of

biotin-polyethylene glycol-poly lactic acid-co-glycolic acid (BIO-PEG–PLGA) and lactic acid-polyethylene glycol-poly lactic acid-co-glycolic acid (LAC-PEG–PLGA), coined BIO-PEG–PLGA/LAC-PEG–PLGA, were produced at Tianjin Medical University; (2) ICG-loaded biodegradable nanoparticles self-assembled from the copolymer of polyethylene glycol–poly lactic acid-co-glycolic acid (PEG-PLGA) were produced at Tianjin Medical University; (3) ICG-loaded shell-sheddable and non-biodegradable nanoparticles self-assembled from two copolymers of pCBAA30-b-pAGA10 (synthesis of poly(carboxybetaine acrylate)-block-poly(2-acrylamido glucopyranose)) and pLAMA30-b-pAAPBA20 (synthesis of poly(2-lactobionamidoethyl methacrylate)–block-poly(3-acrylamidophenylboronic acid)), coined pCA/pLB Nps, were produced at Nankai University. All solvents were of analytical grade and used without further purification.

Preparation of Three Types of ICG-Loaded Nanoparticles

In brief, three types of nanoparticles as carriers loaded in ICG were prepared by the nano-precipitation method. To evaluate ICG loading and encapsulation efficiency, 1.0 ml of the three types of ICG-loaded nanoparticle suspensions was centrifuged and the supernatants were analyzed at 784 nm using a fluorescence spectrometer (RF-5301PC, Shimadzu, Japan).

Dynamic Diffuse Fluorescence Tomography System

Figure 1 shows a schematic diagram of our designed dynamic DFT system. The performance of the system has been evaluated by dynamic phantom experiments and ICG pharmacokinetic assessment of healthy mouse livers [19–21]. In this system, the mouse was placed in a chamber that was fixed on a rotation stage for achieving different spatial sampling densities. The laser light source with a 780-nm excitation wavelength propagated throughout the mouse and was collected by detection fibers which were coupled into a fiber switch. Subsequently, the outputs of the fiber switch were fed into the filter wheels for separating excitation and emission light. Finally, the light signals were detected using PMTs and a photon counting module.

In this work, each mouse was rotated continuously for multiple circles at a fixed Z-coordinate to dynamically monitor the metabolism process of ICG on the imaging plane of the tumor within 24 h. These circles, corresponding to a series of two-dimensional fluorescence tomographic images, were obtained by DFT reconstruction. For each circle, the mouse was rotated 360°, and 16 projections were acquired with an angular increment of 22.5°. The acquisition time for collecting one circle of projection data was approximately 1 min. In the *in vivo* experiments, the dynamic DFT measurement was commenced at 2 min after intravenous injection.

Animals

All mice were purchased from Beijing HFK Bioscience Co., Ltd. (Beijing, China), and all protocols for animal experiments were generated according to the guidelines of the Council for the Purpose of Control and Supervision of Experiments on Animals, Ministry of Public Health, Government of China. In the *in vivo* experiments, twelve seven-week-old male Balb/c nude mice (weighing about 13–19 g) with HepG2/ADR hepatocellular carcinoma and a tumor

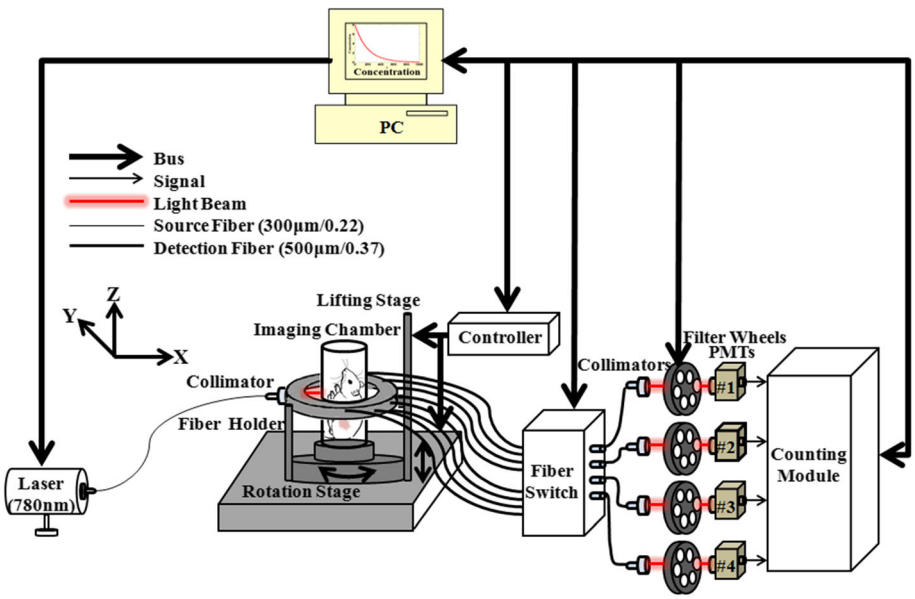

Fig. 1. Schematic diagram of the dynamic DFT system.

volume of approximately 100 mm^3 xenografted on the legs were randomly divided into four groups ($n = 3$ per group). The experimental process before DFT measurement was as follows: (1) each mouse was anesthetized with 10 % chloral hydrate at a dose of 300 mg/kg body weight through the abdominal cavity [22, 23]; (2) the mouse was hung in a polyformaldehyde cylinder chamber with a diameter of 30 mm surrounded by matching fluid (1 % intralipid) [24]; (3) 400 μl of three types of ICG-loaded nanoparticles (content of ICG: 50 μg/ml) and free ICG (50 μg/ml) were intravenously injected into the mice in each group, respectively. Afterwards, an *in vivo* pharmacokinetic analysis was performed 2–11 min, 30 min, 1, 2, 3, 4, 6, 8, 10, 12, and 24 h post-injection, respectively. Particularly noteworthy, the optical signal measurements were performed pre- and post-injection of ICG, respectively. As a result, the background noise could be reduced by calibration.

Frozen Tumor Sections

After the end of the dynamic DFT measurement, all mice were euthanized *via* intraperitoneal injection of 10 % chloral hydrate at a dose of 1.5 g/kg body weight [22, 23]. The euthanized mice were frozen in a refrigerator for 12 to 24 h. Using a tube as a mold, the frozen mice were then embedded in a 1:1 mixture of sucrose solution at a dose of 20 g/l and optimal cutting temperature medium (SAKURA 4583, SAKURA, Japan) [25]. The frozen mice were then placed inside a freezing microtome (CM1950, Leica, Germany) to obtain slice images. Here, the mice were sectioned axially.

DFT Reconstruction Method and Pharmacokinetic Analysis

To obtain the pharmacokinetic rates of ICG in tumor, the method involves two main steps including recovering a sequence of fluorescence distributions using DFT image reconstruction algorithm and fitting the time course of the average ICG concentration in the tumor region to a two-compartmental model for obtaining the fitting parameters related to pharmacokinetic rates.

In DFT reconstruction, the fluorescence properties can be recovered by using transport model-based image reconstruction algorithm and measurement data from the tissue surface. DFT model with continuous wave excitation point sources can be described by a set of the coupled diffusion equations in turbid media, where the solution of the first equation provides the driving source term of the second [26]:

$$\begin{cases} [\nabla \cdot D_x(\mathbf{r})\nabla - \mu_{ax}(\mathbf{r})c]\Phi_x(\mathbf{r}, \mathbf{r}_s) = -\delta(\mathbf{r} - \mathbf{r}_s) \\ [\nabla \cdot D_m(\mathbf{r})\nabla - \mu_{am}(\mathbf{r})c]\Phi_m(\mathbf{r}, \mathbf{r}_s) = -c\Phi_x(\mathbf{r}, \mathbf{r}_s)\eta\mu_{af}(\mathbf{r}) \end{cases} \quad (1)$$

with the Robin-type boundary conditions on the boundary of the imaging domain Ω:

$$\Phi_v(\mathbf{r}, \mathbf{r}_s) + 2\gamma D_v(r)\mathbf{n} \cdot \nabla \Phi_v\left(\mathbf{r}, \mathbf{r}_s\right)\Big|_{r \in \partial\Omega} = 0 \quad (2)$$

where subscripts x and m denote the excitation and emission wavelengths, respectively; $\Phi_v(\mathbf{r}, \mathbf{r}_s)$ ($v \in [x, m]$) is the photon density; the optical parameters involved are the absorption coefficient $\mu_{av}(\mathbf{r})$, the reduced scattering coefficient $\mu_{sv}'(\mathbf{r})$, and the diffusion coefficient $D_v(\mathbf{r}) = c/3[\mu_{av}(\mathbf{r}) + \mu_{sv}'(\mathbf{r})]$; c is the speed of light in medium; the fluorescence parameter is the fluorescent yield $\eta\mu_{af}(\mathbf{r})$, a product of the fluorophore's quantum efficiency η and its absorption coefficient $\mu_{af}(\mathbf{r})$; $\gamma = (1 + R_f)/(1 - R_f)$ and $R_f \approx -1.4399n^{-2} + 0.7099n^{-1} + 0.6681 + 0.0636n$ are the internal reflection coefficient at the boundary, with $n = 1.4$ being the relative refractive index of tissue to the air. These quantities are generally the functions of the position vector $\mathbf{r}$. Herein, $\mu_{av}(\mathbf{r})$ and $\mu_{sv}'(\mathbf{r})$ used in all experiments were, respectively, set to 0.03 mm^{-1} and 1.0 mm^{-1}, corresponding to the average values of bulk soft tissues [27].

Then, we have an integral equation by use of the normalized Born approach, which links the corrected measurements and the fluorescence yield to be reconstructed, as follows:

$$y(\mathbf{r}_d, \mathbf{r}_s) = \frac{\int_\Omega cG(\mathbf{r}_d, \mathbf{r})\Phi_x(\mathbf{r}, \mathbf{r}_s)\eta\mu_{af}(\mathbf{r})d\Omega}{I_x(\mathbf{r}_d, \mathbf{r}_s)} \quad (3)$$

where $y(\mathbf{r}_d, \mathbf{r}_s)$ is the Born ratio of the emission and excitation intensities measured at a detector position $\mathbf{r}_d$ concerning to the excitation source at $\mathbf{r}_s$; $G(\mathbf{r}_d, \mathbf{r})$ is the density at $\mathbf{r}_d$ for a source at $\mathbf{r}$; $I_x(\mathbf{r}_d, \mathbf{r}_s)$ is the excitation flux at $\mathbf{r}_d$ for a source at $\mathbf{r}_s$.

After numerically performing a discretization procedure by a finite-element method (FEM), the Eq. (3) can be expressed as [26, 28]

$$\mathbf{y} = \mathbf{W} \cdot \mathbf{x} \quad (4)$$

where $\mathbf{y} \in \mathbf{R}^{N_{d\times s}\times 1}$ denotes the Born normalized measurements for all the source-detector pairs; $\mathbf{x} \in \mathbf{R}^{N\times 1}$ is the fluorescence yields to be reconstructed; and $\mathbf{W} \in \mathbf{R}^{N_{d\times s}\times N}$ denotes the weight matrix.

Since the inverse problem is generally ill-posed, the fluorescence yield can be acquired by using the regularization method to stabilize the reconstruction procedure [28].

$$\Phi(\mathbf{x}) = \|\mathbf{y} - \mathbf{W}\mathbf{x}\|_2^2 + \lambda\|\mathbf{L}\mathbf{x}\|_2^2 \quad (5)$$

where λ is the regularization parameter; $\mathbf{L}$ is the regularization matrix that used to constrain the solution to be stable. In this paper, the image reconstruction algorithm based on FEM was developed by our lab, which was implemented using MATLAB software. The imaging plane was divided into 5400 triangular elements corresponding to 2791 nodes,

λ used in all experiments was empirically selected to be 0.2, and $\mathbf{L}$ was set to the identity matrix.

After obtaining fluorescence yield ($\eta\mu_{af}(\mathbf{r})$) image, the ICG concentration C (μM) can be derived by the following formula when it is below 80 μg ml^{-1} in whole blood, which can be expressed at time t [29]:

$$\mu_{af}(t) = \ln 10 \xi C(t) \tag{6}$$

where ξ (0.013 mm^{-1} μM^{-1}) is the extinction coefficient of ICG [30].

Then, the concentration-time curves and fitting parameters of ICG in the mouse tumor can be obtained by a biexponential-curve-fitting method based on a commonly used two-compartment model [31].

$$C(t) = -A\exp(-\alpha t) + B\exp(-\beta t) \tag{7}$$

where A and B (unit: a.u.) are intercepts on $C(t)$ for each exponential segment of the curve; α and β (unit: min^{-1}) represent rate constants for the ICG distribution phase and elimination phase, respectively. In this work, the time course of ICG two-compartment concentrations was fitted by using MATLAB Function nlinfit which is Gauss-Newton method [31].

The two-compartment model of ICG pharmacokinetics in the tumor after intravenous injection can be described mathematically by the following ordinary differential equation sets [32, 33]:

$$\begin{bmatrix} dC_p/dt \\ dC_e/dt \end{bmatrix} = \begin{bmatrix} K_{pe} & -K_{ep}-K_p \\ -K_{pe} & K_{ep} \end{bmatrix} \cdot \begin{bmatrix} C_p \\ C_e \end{bmatrix} \tag{8}$$

where C_p and C_e denote the ICG concentrations in plasma and the extracellular-extravascular space (EES), respectively. C in the above Eq. (7) is the sum of C_p and C_e. The factors K_{pe}, K_{ep}, and K_p are pharmacokinetic rates describing the ICG drainage out of and leakage into the EES, as well as the ICG elimination from the body through the circulatory system, respectively. In this model, the tumor region was assumed to consist of plasma and EES was defined as the region that lies outside of both the vascular region and the tumor cells.

On the basis of Eqs. (7)–(8), the pharmacokinetic rates K_{pe}, K_p, and K_{ep} can be calculated by the following equations [34]:

$$K_{pe} = (-A\beta + B\alpha)/(-A + B) \tag{9}$$

$$K_p = \alpha\beta/K_{pe} \tag{10}$$

$$K_{ep} = \alpha + \beta - K_{pe} - K_p \tag{11}$$

Results

Results of Dynamic DFT

Below, some representative results for each experimental group are demonstrated. Figures 2, 3, 4, and 5 illustrate the cryosection images with a circle marking the tumor position and overlays of cryosection images and the corresponding fluorescence tomographic image sequences reconstructed at 2–11 min, 30 min, 1, 2, 3, 4, 6, 8, 10, 12, and 24 h after injection of ICG-loaded BIO-PEG-PLGA/LAC-PEG-PLGA, ICG-loaded PEG-PLGA, ICG-loaded pCA/pLB Nps, and free ICG, respectively. The acquisition time for collecting one complete frame of the projection data was about 1 min. Deserved to be mentioned, due to the inherently ill-posed nature in solving the inverse problem of DFT, the normally prevalent edge artifacts are obvious in source and detector positions. In addition, ICG as a non-target dye is unable to assemble in the tumor region completely; thus, the reconstructed fluorescence images in the non-tumor region were filtered for accurately calculating the average ICG concentration in the tumor region, that is, we only estimated the average ICG concentrations of the tumor region of reconstructed fluorescence tomographic images for improving pharmacokinetic analysis. The average ICG concentration in the tumor region was utilized to fit parameters related to pharmacokinetic rates. Figure 2 shows that ICG-loaded BIO-PEG-PLGA/LAC-PEG-PLGA slowly congregated in the tumor, decreased over time, and exhibited the same changing trend as ICG-loaded PEG-PLGA shown in Fig. 3. However, the difference was that the former reached a maximum of aggregation at the tumor site approximately 4 h post-injection, while the latter reached a maximum of aggregation after about 6 h. Additionally, we were able to observe that ICG loaded in pCA/pLB Nps quickly accumulated in the tumors and reduced with time as shown in Fig. 4. Here, the same variation trend as free ICG (Fig. 5) was demonstrated. Significantly, we found that the fluorescence intensity of ICG-loaded pCA/pLB Nps in the tumor site was much stronger than that of ICG-loaded BIO-PEG-PLGA/LAC-PEG-PLGA, ICG-loaded PEG-PLGA, and free ICG over 24 h. This finding indicates that the pCA/pLB Nps enabled ICG to enhance the tumor accumulation more efficiently compared to BIO-PEG-PLGA/LAC-PEG-PLGA, PEG-PLGA, and free ICG.

Results of Pharmacokinetic Analysis

According to Eqs. (1)–(5), the ICG concentrations could be achieved by calculating the mean ICG concentration within the tumor region. The ICG concentration-time curves and the corresponding fitting parameters could be obtained by using a Gauss-Newton method to fit the time course after normalizing the ICG concentration based on the two-compartmental model. Figure 6 shows the raw data

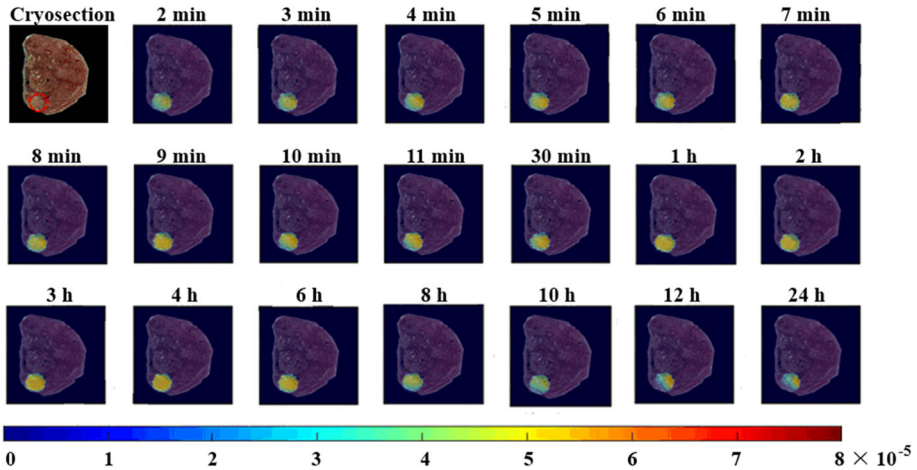

Fig. 2. Cryosection image with a circle marking the tumor position and overlays of fluorescence tomographic image sequences reconstructed at 2–11 min, 30 min, 1, 2, 3, 4, 6, 8, 10, 12, and 24 h after injection of ICG-loaded BIO-PEG-PLGA/LAC-PEG-PLGA.

(makers) and the fitting curves (solid lines) of normalized ICG concentrations at different measurement time points (*i.e.*, 2–11 min, 30 min, 1, 2, 3, 4, 6, 8, 10, 12, and 24 h after injection) for ICG-loaded BIO-PEG-PLGA/LAC-PEG-PLGA, ICG-loaded PEG-PLGA, ICG-loaded pCA/pLB Nps, and free ICG. Our findings indicate that ICG-loaded pCA/pLB Nps tend to aggregate in the tumor tissue rapidly and feature the largest accumulation of ICG compared with other ICG formulations. In addition, each type of ICG-loaded nanoparticle exhibited superior retention capabilities compared to the free ICG. To further analyze the fitting curves, R^2 (R square), $T_{\max}$ (time to reach the maximal fluorescence intensity), and $T_{1/2}$ (half-life time) were calculated as shown in Table 1. All the fitting curves featured a high correlation ($R^2 > 0.92$), indicating the suitable validity of the fitting curves [8]. In terms of $T_{\max}$, we found that ICG-loaded pCA/pLB Nps took the least time (1/20 h) to reach the maximum concentration and the free ICG required a similar period of time (1/12 h). However, ICG-loaded BIO-PEG-PLGA/LAC-PEG-PLGA (4 h) and ICG-loaded PEG-PLGA (6 h) required more time. As for $T_{1/2}$, free ICG required the least amount of time, *i.e.*, 2 h, to decrease by one half of its maximum concentration. Similarly, ICG-loaded pCA/pLB Nps required 4 h. However, both ICG-loaded BIO-PEG-PLGA/LAC-PEG-PLGA and ICG-loaded PEG-PLGA maintained high concentrations, *i.e.*, over half of its maximum concentration value, until 24 h.

According to Eqs. (6)–(11), the pharmacokinetic rates, K_{pe}, K_{ep}, and K_p (mean ± SD, for $n = 3$ per group), of those four ICG formulations could be calculated as summarized in Table 2. We could see that the K_{pe} (EES drainage) of ICG-loaded BIO-PEG-PLGA/LAC-PEG-PLGA, ICG-loaded PEG-PLGA, and ICG-loaded pCA/pLB Nps were 1.54 ±

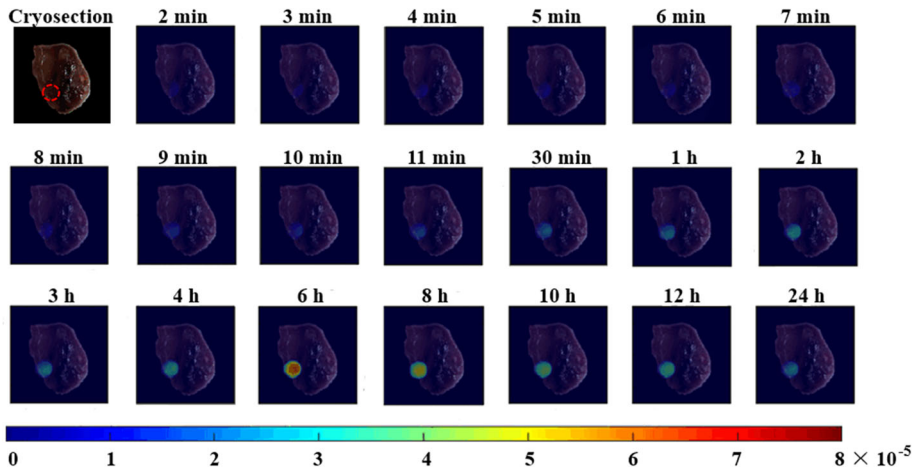

Fig. 3. Cryosection image with a circle marking the tumor position and overlays of fluorescence tomographic image sequences reconstructed at 2–11 min, 30 min, 1, 2, 3, 4, 6, 8, 10, 12, and 24 h after injection of ICG-loaded PEG-PLGA.

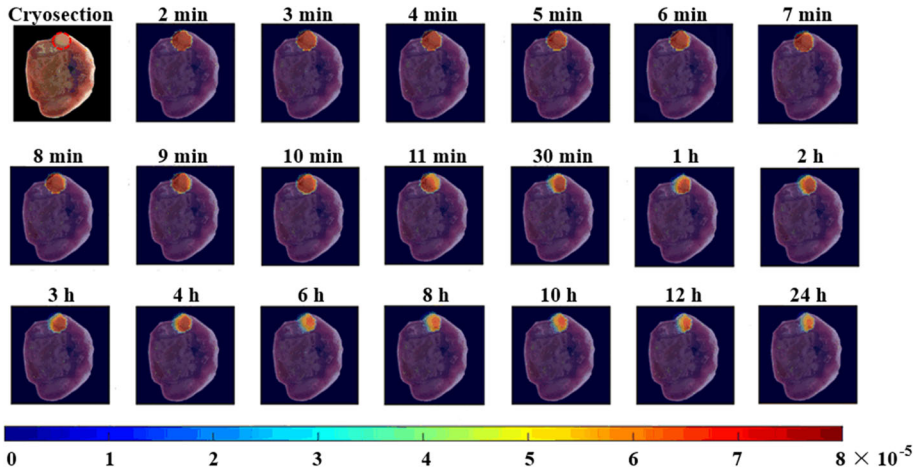

Fig. 4. Cryosection image with a circle marking the tumor position and overlays of fluorescence tomographic image sequences reconstructed at 2–11 min, 30 min, 1, 2, 3, 4, 6, 8, 10, 12, and 24 h after injection of ICG-loaded pCA/pLB Nps.

0.212, 1.34 ± 0.301, and 3.94 ± 0.154 $min^{-1}10^{-2}$, respectively, were larger than that of free ICG (0.47 ± 0.019 $min^{-1}10^{-2}$), suggesting that the nanostructures effectively enhanced ICG tumor accumulation. The K_{ep} (leakage into EES) of ICG-loaded pCA/pLB Nps and free ICG were 4.14 ± 0.353 and 1.32 ± 0.183 $min^{-1}10^{-2}$, respectively, while ICG-loaded BIO-PEG-PLGA/LAC-PEG-PLGA and ICG-loaded PEG-PLGA demonstrated negative values of -0.46 ± 0.031 and -0.75 ± 0.104 $min^{-1}10^{-2}$, respectively. This latter finding was due to the slow metabolic velocity after reaching the maximum accumulation compared with the prior two formulations. The K_p of ICG-loaded BIO-PEG-PLGA/LAC-PEG-PLGA and ICG-loaded PEG-PLGA were 2.23 ± 0.391 and 1.59 ± 0.288 $min^{-1}10^{-4}$, respectively. And the values of ICG-loaded pCA/pLB Nps and free ICG were 8.76 ± 0.455 and 2.89 ± 0.323 $min^{-1}10^{-4}$, respectively.

Discussion

We have investigated the biodistribution of ICG in tumor-bearing mice after single intravenous injection of three types of ICG-loaded nanoparticles and free ICG solution in combination with dynamic DFT. The pharmacokinetic rates of these four ICG formulations were investigated and combined with the two-compartment model by analyzing pharmacokinetics. Figures 2, 3, 4, and 5 show that ICG concentrations in the tumors were significantly higher (2–5 times) when delivered *via* nanoparticles than when administered as free ICG. Moreover, the ICG concentrations in the tumors were significantly higher within 24 h. This finding demonstrated the capability of nanoparticles to enhance the accumulation amount and retention time in the tumor tissues [35]. From inspection of Tables 1 and 2, we could see that the biodegradable nanoparticles of BIO-PEG-PLGA/LAC-

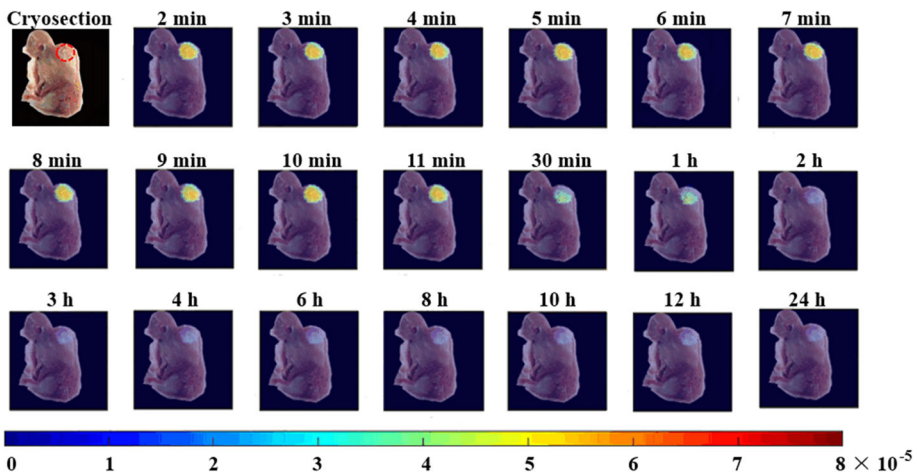

Fig. 5. Cryosection image with a circle marking the tumor position and overlays of fluorescence tomographic image sequences reconstructed at 2–11 min, 30 min, 1, 2, 3, 4, 6, 8, 10, 12, and 24 h after injection of free ICG.

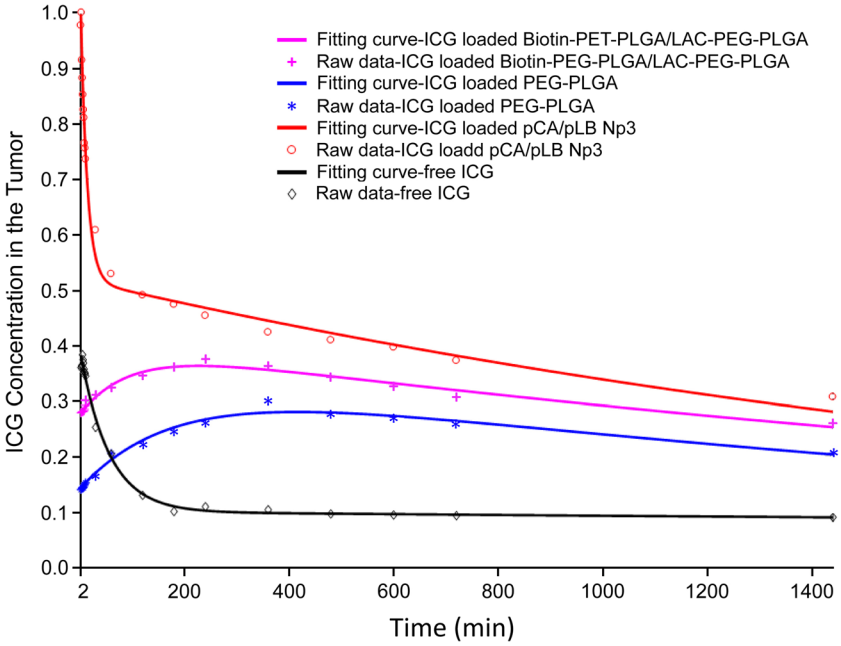

Fig. 6. Fitting curves of ICG concentrations *vs.* time for tumors injected with ICG-loaded BIO-PEG-PLGA/LAC-PEG-PLGA, ICG-loaded PEG-PLGA, ICG-loaded pCA/pLB Nps, and free ICG over 24 h.

PEG-PLGA and PEG-PLGA exhibited large T_{max} values which are in accordance with other reported references [36, 37]. Moreover, the K_{pe} values of BIO-PEG-PLGA/LAC-PEG-PLGA were larger than that of PEG-PLGA due to its positive tumor-targeting ability. The biodegradable nanoparticles were able to not only improve the drug delivery in tumor site but also avail the excretion of the metabolite, which could reduce the damage to host tissues [36, 37]. Nevertheless, pCA/pLB Nps as a new type of shell-sheddable nanoparticle demonstrated fast accumulation and prolonged retention in contrast to the other two nanoparticle types. The shell-sheddable nanoparticles could reach tumor sites *via* the EPR effect and exposure to tumor microenvironment responding to specific stimuli in the tumor after systemic administration, leading to a burst release of the drug [38–40]. In particular, the shell-detachable pCA/pLB Nps were designed to bury or protect the functional group while it is in the circulatory system, and the shield can then be removed when exposed to a specific tumor microenvironment, which had been proved to make the chance of functional groups to recognize and target the tumor cells as well as enhance the cellular internalization. In addition, we found that the pharmacokinetic rate values demonstrated some difference in each experimental group. This difference may have been caused by the different experimental conditions and physiological status of the mice. Moreover, guaranteeing the same measurement parameters during the entire measurement procedure was vital since it was always necessary to remove the mice from the chamber for the administration of anesthetics.

In this work, the fluorescence excitation and emission wavelengths of ICG were deemed unchangeable since the *in vivo* experiments were conducted within 24 h. Correspondingly, the ICG extinction coefficient related to the wavelength was also regarded as a constant. The proposed strategy for the image reconstruction could be considered an indirect method, including DFT image reconstruction and compartmental model fitting. For fully characterizing the ICG pharmacokinetic process, improving the dynamic measurement capability or adopting a direct reconstruction method by incorporating a kinetic model to the inversion procedure efficiently reduced errors in the process of reconstructing the interim ICG concentrations.

Table 1. Corresponding parameters (R^2, T_{max}, and $T_{1/2}$) of the fitting curves in Fig. 6

ICG solution types	R^2	T_{max} (h)	$T_{1/2}$ (h)
ICG-loaded BIO-PEG-PLGA/LAC-PEG-PLGA	0.93	4	> 24
ICG-loaded PEG-PLGA	0.94	6	> 24
ICG-loaded pCA/pLB Nps	0.94	1/20	6
Free ICG	0.96	1/12	2

Table 2.. Mean ± SD of ICG pharmacokinetic-rates in HepG2 tumor-bearing mice 24 h after intravenous injection ($n = 3$ in each group)

ICG solution types	K_{pe} ($min^{-1}10^{-2}$)	K_{ep} ($min^{-1}10^{-2}$)	K_p ($min^{-1}10^{-4}$)
ICG-loaded BIO-PEG-PLGA/LAC-PEG-PLGA	1.54 ± 0.212	− 0.46 ± 0.031	2.23 ± 0.391
ICG-loaded PEG-PLGA	1.34 ± 0.301	− 0.75 ± 0.104	1.59 ± 0.288
ICG-loaded pCA/pLB Nps	3.94 ± 0.154	4.14 ± 0.353	8.76 ± 0.455
Free ICG	0.47 ± 0.019	1.32 ± 0.183	2.89 ± 0.323

Conclusions

In this study, a real-time study to assess the pharmacokinetics of three different ICG-loaded nanoparticles and free ICG in tumor-bearing mice based on a proposed dynamic DFT system was carried out. The DFT technology presented here provided real-time tomographic images on the spatial level, and pharmacokinetic rates for the semi-quantitative assessment of the pharmacokinetics of nanoparticles at the tumor site using this pharmacokinetic analysis method could be derived. Furthermore, this feasibility study represents the first step in exploring the potential applications of dynamic DFT in the pharmacokinetic assessment of nanoparticles by loading ICG, which could be used to evaluate the anti-tumor effect of therapeutic nano-drugs or nano-related pharmaceutical drugs in mice or other small animals. In addition, this method can also be extended to other fields, such as the monitoring of disease progression, the evaluation of novel therapies, *etc.*

Acknowledgments. The authors would like to acknowledge funding support from the National Natural Science Foundation of China and Tianjin Municipal Government of China.

Funding. This study was funded by the National Natural Science Foundation of China (61475115, 81671728, 61475116, 61575140, 81571723, 81771880) and Tianjin Municipal Government of China (17JCZDJC32700, 18JCYBJC29400).

Compliance with Ethical Standards

Conflict of Interest

The authors declare that they have no conflict of interest.

Ethical Approval

All applicable institutional and/or national guidelines for the care and use of animals were followed.

References

1. Matsumura Y, Kataoka K (2009) Preclinical and clinical studies of anticancer agent-incorporating polymer micelles. Cancer Sci 100:572–579
2. Jokar S, Pourjavadi A, Adeli M (2014) Albumin-graphene oxide conjugates; carriers for anticancer drugs. RSC Adv 4:33001–33006
3. Kim TY, Kim DW, Chung JY, Shin SG, Kim SC, Heo DS, Kim NK, Bang YJ (2004) Phase I and pharmacokinetic study of Genexol-PM, a cremophor-free, polymeric micelle-formulated paclitaxel, in patients with advanced malignancies. Clin Cancer Res 10:3708–3716
4. Gabizon AA (2001) Pegylated liposomal doxorubicin: metamorphosis of an old drug into a new form of chemotherapy. Cancer Investig 19:424–436
5. Tang S, Meng QS, Sun HP, Su J, Yin Q, Zhang Z, Yu H, Chen L, Gu W, Li Y (2017) Dual pH-sensitive micelles with charge-switch for controlling cellular uptake and drug release to treat metastatic breast cancer. Biomaterials 114:44–53
6. Song WT, Tang ZH, Zhang DW, Zhang Y, Yu H, Li M, Lv S, Sun H, Deng M, Chen X (2014) Anti-tumor efficacy of c(RGDfK)-decorated polypeptide-based micelles co-loaded with docetaxel and cisplatin. Biomaterials 35:3005–3014
7. Zhao X, Yang CX, Chen LG, Yan XP (2017) Dual-stimuli responsive and reversibly activatable theranostic nanoprobe for precision tumor-targeting and fluorescence-guided photothermal therapy. Nat Commun 8:14998
8. Wang R, Zhou L, Wang WX, Li X, Zhang F (2017) In vivo gastrointestinal drug-release monitoring through second near-infrared window fluorescent bioimaging with orally delivered microcarriers. Nat Commun 8:14702
9. Tao ZM, Dang XN, Huang X, Muzumdar MD, Xu ES, Bardhan NM, Song H, Qi R, Yu Y, Li T, Wei W, Wyckoff J, Birrer MJ, Belcher AM, Ghoroghchian PP (2017) Early tumor detection afforded by in vivo imaging of near-infrared II fluorescence. Biomaterials 134:202–205
10. Wan H, Yue JY, Zhu SJ, Uno T, Zhang X, Yang Q, Yu K, Hong G, Wang J, Li L, Ma Z, Gao H, Zhong Y, Su J, Antaris AL, Xia Y, Luo J, Liang Y, Dai H (2018) A bright organic NIR-II nanofluorophore for three dimensional imaging into biological tissues. Nat Commun 9:1171
11. Simon GH, Daldrup-Link HE, Kau J, Metz S, Schlegel J, Piontek G, Saborowski O, Demos S, Duyster J, Pichler BJ (2006) Optical imaging of experimental arthritis using allogeneic leukocytes labeled with a near-infrared fluorescent probe. Eur J Nucl Med Mol Imaging 33:998–1006
12. Rudin M, Weissleder R (2003) Molecular imaging in drug discovery and development. Nat Rev Drug Discov 2:123–131
13. Schulz RB, Ale A, Sarantopoulos A, Freyer M, Soehngen E, Zientkowska M, Ntziachristos V (2010) A hybrid system for simultaneous fluorescence and x-ray computed tomography. IEEE Trans Med Imaging 29:465–473
14. Liu X, Zhang B, Luo JW, Bai J (2012) 4-D reconstruction for dynamic fluorescence diffuse optical tomography. IEEE Trans Med Imaging 31:2120–2132
15. Saxena V, Sadoqi M, Shao J (2004) Indocyanine green-loaded biodegradable nanoparticles: preparation, physicochemical characterization and in vitro release. Int J Pharm 278:293–301
16. Pichette J, Lapointe E, Bérubé-Lauzière Y (2008) Time-domain 3D localization of fluorescent inclusions in a thick scattering medium. Proc SPIE 7099:709907–1–709907–12
17. Alacam B, Yazici B, Intes X, Nioka S, Chance B (2008) Pharmacokinetic-rate images of indocyanine green for breast tumors using near-infrared optical methods. Phys Med Biol 53:837–859
18. Liu X, Guo XL, Liu F et al (2011) Imaging of indocyanine green perfusion in mouse liver with fluorescence diffuse optical tomography. IEEE Trans Biomed Eng 58:2139–2143
19. Zhang YQ, Zhang LM, Yin GY, Ma W, Gao F (2018) Assessing indocyanine green pharmacokinetics in mouse liver with a dynamic diffuse fluorescence tomography system. J Biophotonics 11:e201800041. https://doi.org/10.1002/jbio.201800041
20. Zhang YQ, Wang X, Yin GY et al (2017) Dynamic experimental system for indocyanine green pharmacokinetic imaging. Chinese J Lasers 44:0107001–1–0107001-7
21. Zhang YQ, Wang X, Yin GY et al (2016) Preliminary experiments on pharmacokinetic diffuse fluorescence tomography of CT-scanning mode. Proc SPIE 10024:100242Y-1–100242Y-7

22. Sisson DF, Siegel J (1989) Chloral hydrate anesthesia: EEG power spectrum analysis and effects on VEPs in the rat. Neurotoxicol Teratol 11:51–56
23. Field KJ, White WJ, Lang CM (1993) Anaesthetic effects of chloral hydrate, pentobarbitone and urethane in adult male rats. Lab Anim 27:258–269
24. Wan WB, Wang YH, Qi J, Liu L, Ma W, Li J, Zhang L, Zhou Z, Zhao H, Gao F (2016) Region−based diffuse optical tomography with registered atlas: in vivo acquisition of mouse optical properties. Biomed Opt Express 7:5066–5080
25. Sarantopoulos A, Themelis G, Ntziachristos V (2011) Imaging the bio-distribution of molecular probes using multispectral cryoslicing imaging. Mol Imag Biol 13:874–885
26. Gao F, Zhao HJ, Yamada Y et al (2006) A linear, featured-data scheme for image reconstruction in time-domain fluorescence molecular tomography. Opt Express 14:7109–7124
27. Hyde D, Schulz R, Brooks D, Miller E, Ntziachristos V (2009) Performance dependence of hybrid x-ray computed tomography/fluorescence molecular tomography on the optical forward problem. J Opt Soc Am A 26:919–923
28. Ale A, Schulz RB, Sarantopoulos A, Ntziachristos V (2010) Imaging performance of a hybrid x-ray computed tomography-fluorescence molecular tomography system using priors. Med Phys 37(5):1976–1986
29. Biesen PRVD, Jongsma FH, Tangelder GJ, Slaaf DW (1995) Yield of fluorescence from indocyanine green in plasma and flowing blood. Ann Biomed Eng 23:475–481
30. Landsman MLJ, Kwant G, Mook GA, Zijlstra WG (1976) Light-absorbing properties, stability, and spectral stabilization of indocyanine green. J Appl Physiol 40:575–583
31. Shinohara H, Tanaka A, Kitai T, Yanabu N, Inomoto T, Satoh S, Hatano E, Yamaoka Y, Hirao K (1996) Direct measurement of hepatic indocyanine green clearance with near-infrared spectroscopy: separate evaluation of uptake and removal. Hepatology 23:137–144
32. Zhang GL, Liu F, Zhang B, He Y, Luo J, Bai J (2013) Imaging of pharmacokinetic rates of indocyanine green in mouse liver with a hybrid fluorescence molecular tomography/x-ray computed tomography system. J Biomed Opt 18:040505
33. Alacam B, Yazici B, Intes X, Chance B (2006) Extended Kalman filtering for the modeling and analysis of ICG pharmacokinetics in cancerous tumors using NIR optical methods. IEEE T Biomed Eng 53:1861–1871
34. Shargel L, Susanna WP, Andrew BCY (2004) Applied biopharmaceutics and pharmacokinetics, 5th edn. McGraw-Hill Medical, New York, pp 62–86
35. Saxena V, Sadoqi M, Shao J (2006) Polymeric nanoparticulate delivery system for Indocyanine green: biodistribution in healthy mice. Int J Pharm 308:200–204
36. Singh Y, Durga KK, Kumar JA et al (2017) Click biotinylation of PLGA template for biotin receptor oriented delivery of doxorubicin hydrochloride in 4T1 cell induced breast cancer. Mol Pharm 14:2749–2765
37. Patel B, Gupta V, Ahsan F (2012) PEG-PLGA based large porous particles for pulmonary delivery of a highly soluble drug, low molecular weight heparin. J Control Release 162:310–320
38. Thambi T, Park JH (2014) Recent advances in shell-sheddable nanoparticles for cancer therapy. J Biomed Nanotechnol 10:1841–1862
39. Du JZ, Du XJ, Mao CQ, Wang J (2011) Tailor-made dual pH-sensitive polymer-doxorubicin nanoparticles for efficient anticancer drug delivery. J Am Chem Soc 133:17560–17563
40. Sun CY, Shen S, Xu CF, Li HJ, Liu Y, Cao ZT, Yang XZ, Xia JX, Wang J (2015) Tumor acidity-sensitive polymeric vector for active targeted siRNA delivery. J Am Chem Soc 137:15217–15224